Optics Communications 437 (2019) 81–89

Contents lists available at ScienceDirect

Optics Communications

journal homepage: www.elsevier.com/locate/optcom

Nadir and omnidirectional limb imaging spectrometer based on acousto-optic tunable filter

Xiaoheng Wang [a,b], Xing Zhong [a,c,*], Ruifei Zhu [a,c], Fang Gao [c]

[a] Changchun Institute of Optics, Fine Mechanics and Physics, Chinese Academy of Sciences, Changchun, 130033, China
[b] University of Chinese Academy of Sciences, Beijing, 100049, China
[c] Chang Guang Satellite Technology CO, LTD, Key Laboratory of Satellite Remote Sensing, Application Technology of Jilin Province, Changchun, 130000, yChina,

ARTICLE INFO

Keywords:
Acousto-optical devices
Remote sensing and sensors
Lens system design
Optical design of instruments

ABSTRACT

Imaging spectrometers for atmospheric detection usually split the beam by using prisms or gratings. However, owing to their spectroscopic principle, these spectrometers can only detect the atmosphere via single mode and single detection. The acousto-optic tunable filter (AOTF) is an electronic filter developed based on the acousto-optic effect of crystal with a field of view that is not limited by the slit. This paper introduces the spectroscopic principle of the AOTF and deduces its diffraction equation. By using the AOTF as a spectroscopic device, this paper also designs a new imaging spectrometer for atmospheric detection. This spectrometer has two fields of view and can detect the hyperspectral atmospheric data in 10° nadir field of view, 360° limb field of view, and 0 km to 100km limb height. The optical system of this imaging spectrometer comprises a front objective lens, an AOTF spectroscopic system, and a relay lens. As an instrument for atmospheric, this spectrometer has the characteristics of dual observation modes, full coverage in the limb field of view, and high spectral resolution.

1. Introduction

The solar spectrum interacts with atmospheric molecules when passing through the atmosphere, thereby affecting the radiation intensity of the solar spectrum. In this case, atmospheric composition information can be obtained by detecting and interpreting the solar radiation spectrum that is transmitted in the atmosphere. Among the many existing atmospheric detection methods, space-based detection is the only approach that guarantees a large coverage and time continuity. Spaceborne hyperspectral instruments generally comprise imaging systems and spectrometers, while spectrometers separate light by using gratings or prisms. Fig. 1 presents a schematic of traditional hyperspectral instruments. The object is focused on the image plane after the imaging system, and a slit is placed on the position of the first image plane as the field diaphragm of the whole system. The spectrometer divides the light from the silt into several spectra [1–3].

Spaceborne atmospheric remote sensing instruments often use nadir or limb detection modes [4,5]. As seen in Fig. 1, prism/grating spectrometers can only perform imaging in a strip-shaped field of view due to the limitations imposed by their spectroscopic principle. Therefore, most hyperspectral imaging instruments only have a single direction and a single mode, that is, they can only detect one direction of the nadir or limb fields of view. Consequentially, traditional atmospheric detection methods only obtain a very limited amount of information and cannot simultaneously detect the total amount and height distribution of the atmosphere. In our previous work, we designed a dual-mode atmospheric detection instrument that not only can simultaneously detect the nadir and limb fields of view by using a multi-functional panoramic annular lens (PAL) but also has a 360° limb mode field of view. The effective image plane of this instrument is a central bright spot (representing the atmospheric data of the nadir field) surrounded by a circle (representing the atmospheric data of the limb field) [6]. This detection method improves the detection efficiency to some extent. However, given that the image plane shape of the detection method is not a long strip, a slit cannot be placed on the image plane and the solar radiation cannot be separated by using a grating or prism. In our previous work, we also used a stepper motor to push different filters for spectral selection. This spectroscopic method can only provide several spectral channels, which cannot satisfy the inversion needs for many atmospheric or aerosol molecules.

The acousto-optic tunable filter (AOTF) is an electronic control filter developed based on the acousto-optic effect of an anisotropic crystal. As shown in Fig. 2, the AOTF comprises a crystal, a piezo-transducer, and an acoustic absorber. Different electrical signals are applied to the piezoelectric transducers, which then convert these signals into ultrasonic signals. These ultrasonic waves enter the crystal and interact with the light transmitted within. This light is diffracted when the Bragg diffraction conditions are satisfied. The acoustic absorber absorbs the residual ultrasonic waves transmitted in the crystal to prevent them from

* Corresponding author at: Changchun Institute of Optics, Fine Mechanics and Physics, Chinese Academy of Sciences, Changchun, 130033, China.
E-mail addresses: wangxiaoheng0013@163.com (X. Wang), ciomper@163.com (X. Zhong).

https://doi.org/10.1016/j.optcom.2018.12.037
Received 24 October 2018; Received in revised form 28 November 2018; Accepted 8 December 2018
Available online 14 December 2018

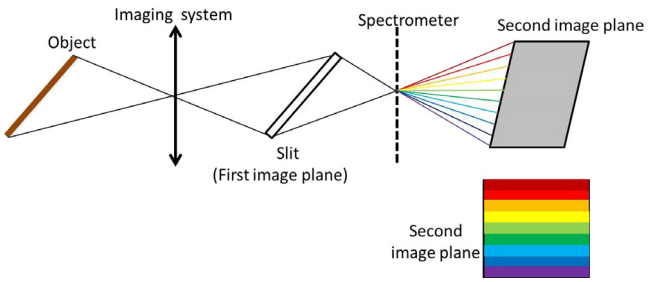

Fig. 1. Schematic of traditional imaging spectrometers.

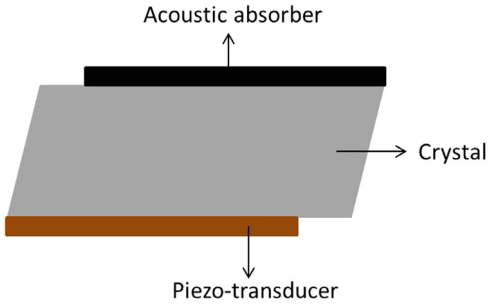

Fig. 2. Structure of the AOTF.

being reflected back and interfere with the normal beam transmission. In this case, different electrical signals can be inputted into the AOTF at different times to achieve the purpose of spectrum selection [7–9]. Unlike traditional spectroscopic instruments, the spectroscopic principle of the AOTF avoids the use of the slit and allows the detection of the spatial atmosphere in multiple modes, multiple directions, and hyperspectral.

In this paper, we deduced the diffraction equation of the AOTF and analyzed its effect on imaging. Based on our findings, we designed a hyperspectral atmospheric remote sensing instrument that can simultaneously detect the hyperspectral solar radiation in the nadir and omnidirectional limb fields of view. This instrument has a detection band ranging from 450 nm to 800 nm as well as shows a higher spatial coverage and detection efficiency compared with traditional hyperspectral detection instruments.

2. Spectroscopy principle of the AOTF

2.1. Acousto-optic effects of the AOTF

Fig. 3 illustrates the diffraction principle of the AOTF. The incident angle of the beam is θ_i, while the wave vector is denoted by k_i. When an ultrasonic signal is applied to the crystal, the beam is diffracted at an angle of θ_d. The relationship among diffraction wave vector k_d, incident wave vector k_i, and ultrasonic wave vector k_a is determined as follows by the vector synthesis rule:

$$\vec{k}_d = \vec{k}_i + \vec{k}_a. \tag{1}$$

The absolute values of each wave vector in Eq. (1) are

$$|k_i| = \frac{2\pi n_i}{\lambda_0},\ |k_d| = \frac{2\pi n_o}{\lambda_0},\ \text{and}\ |k_a| = \frac{2\pi}{\Lambda}, \tag{2}$$

where n_i is the refractive index of incident light, n_o is the ordinary refractive index of diffracted light, λ_0 is the vacuum wavelength, and Λ is the ultrasonic wavelength.

Fig. 3 shows that the relationship of the absolute values of the wave vectors is

$$|k_a|^2 = |k_d|^2 + |k_i|^2 - 2|k_d||k_i|\cos(\theta_i - \theta_d). \tag{3}$$

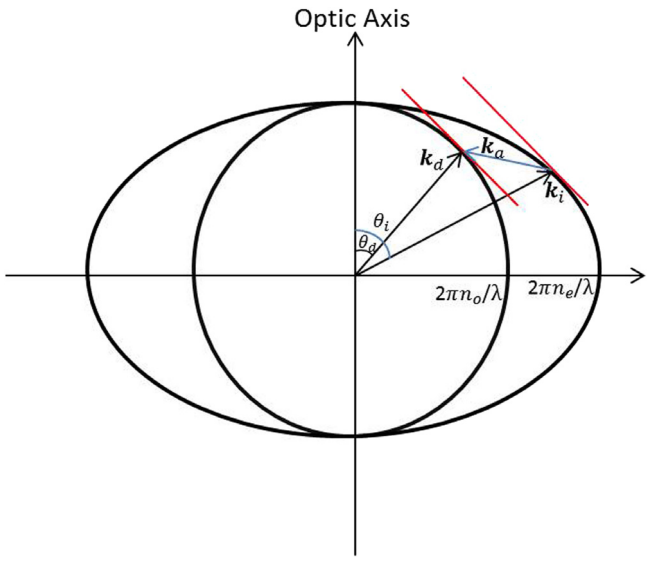

Fig. 3. Wave-vector diagram of the AOTF.

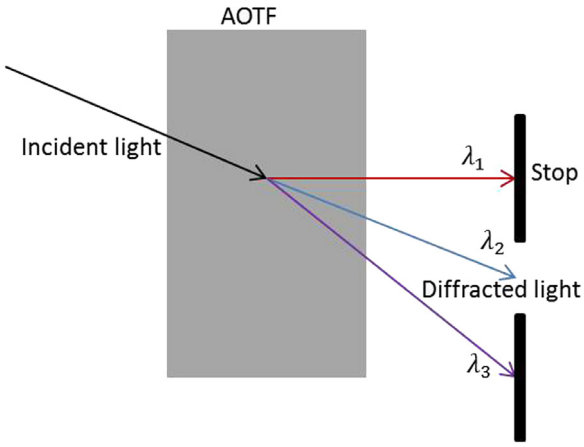

Fig. 4. AOTF diffraction pattern.

Combining Eqs. (2) and (3) yields

$$\frac{\lambda_0^2}{\Lambda^2} = n_0^2 + n_i^2 - 2n_0 n_i \cos(\theta_i - \theta_d), \tag{4}$$

which shows that the diffracted wave λ_0 changes along with the diffraction angle θ_d for the same ultrasonic wave.

2.2. AOTF diffraction equation

Section 2.1 shows that the ultrasonic waves can cause a light diffraction in the crystal and that any diffracted light has its own diffraction angle. As shown in Fig. 4, a stop is placed at a specific position behind the crystal, thereby allowing the beam to pass through a certain diffraction angle. In this case, the exit spectrum changes along with the ultrasonic waves, thereby realizing the purpose of splitting light in time.

We simplify Eq. (4) and use λ instead of λ_0 to represent any wavelength. We rewrite Eq. (4) as

$$\lambda = \Lambda\sqrt{n_0^2 + n_i^2 - 2n_0 n_i \cos(\theta_i - \theta_d)}. \tag{5}$$

Given that only the beam with a fixed diffraction angle can exit the AOTF, $\sqrt{n_0^2 + n_i^2 - 2n_0 n_i \cos(\theta_i - \theta_d)}$ is approximately constant over a

Table 1
Main specifications of the spectrometer.

Parameters	Nadir field of view	Limb field of view
Focal length	7.5 mm	4 mm
Field of view	10°	360° × (53.1°–56°)
F number	6.5	6.5
Band range	450 nm–800 nm	450 nm–800 nm
Spectral resolution	1.5 nm	1.5 nm
Distortion	<1%	<1%
MTF	>0.5@38.5 lp/mm	>0.5@38.5 lp/mm

range of wavelengths. We replace this equation by the constant d_a and rewrite Eq. (5) as

$$\lambda = d_a \Lambda, \tag{6}$$

which is similar to the diffraction equation of gratings. In this case, we call Eq. (6) the diffraction equation of the AOTF. The diffraction wavelength of the grating is proportional to the sine of the diffraction angle, while the diffraction wavelength of the AOTF is proportional to the ultrasonic wavelength. The desired spectrum can be obtained by applying the corresponding ultrasonic wave to the AOTF.

3. Nadir and omnidirectional imaging spectrometer design

3.1. Specifications of the imaging spectrometer

We require an atmospheric imaging spectrometer that can simultaneously detect nadir and omnidirectional limb fields of view. Fig. 5 illustrates the detection mode of this spectrometer. The orbital altitude of the spaceborne spectrometer is assumed to be 1000 km, the nadir field of view α is 10°, the observation range at limb height ranges from 0 km to 100 km, and the distance S from the spectrometer to the limb area is 2000 km. From the geometrical relationship, we deduce that the limb half field of view β ranges from 53.1° to 56°. We need the spatial resolutions of the nadir and limb fields of view to be 2 km and 6 km, respectively. We use the CCD with a pixel size of 13 μm as the detector of the imaging spectrometer. Therefore, the focal lengths of the nadir and limb fields of view then become 7.5 mm and 4 mm, respectively. This spectrometer aims to detect atmosphere components, such as water vapor, ozone, oxygen molecules and some pollutants, which have the characteristic lines in the visible light range. In addition, with a relative high transmittance at the range of the visible spectrum, the self-designed optical system is able to realize the accurate detection of cloud maps. The AOTF satisfied the spectral was selected with the spectral range of 450 nm~800 nm with the spectral resolution of 1.5 nm. Table 1 shows the main specifications of the imaging spectrometer.

3.2. Structure of the imaging spectrometer

The AOTF uses two structures for spectral separation, namely, the parallel light and the telecentric light incident AOTF [10]. The half field angle of the spectrometer reaches up to 56°, and the parallel beam incident AOTF can cause the beam to have a large aperture, thereby making the AOTF and other optical elements unable to be processed. Therefore, we select the telecentric light incident AOTF.

Fig. 6 shows the optical structure of the imaging spectrometer based on the telecentric beam incident AOTF, which comprises a front objective lens, an AOTF spectroscopy system, and a relay lens [11]. The telecentric beam enters the AOTF after passing through the front objective lens. After the AOTF selects the desired spectrum, the relay lens images the selected spectrum on the focal plane.

The imaging system only has two projection modes, namely, tangent projection and equidistance projection. The half limb field angle of the spectrometer is 56°, while its limb focal length is 4 mm. The half image heights of tangent projection and the equidistant projection are 5.93 mm and 3.90 mm, respectively. The equidistance projection has

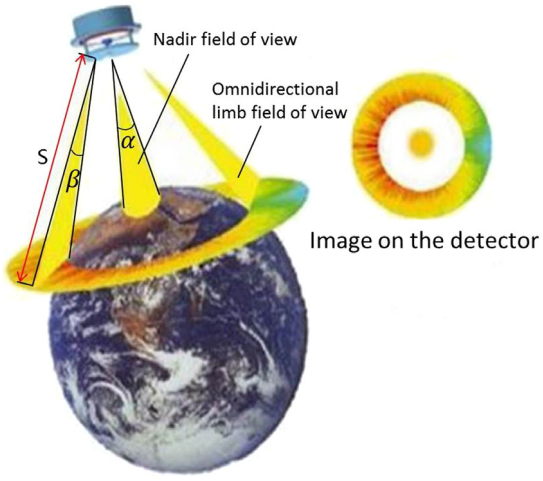

Fig. 5. Detection mode of the spectrometer.

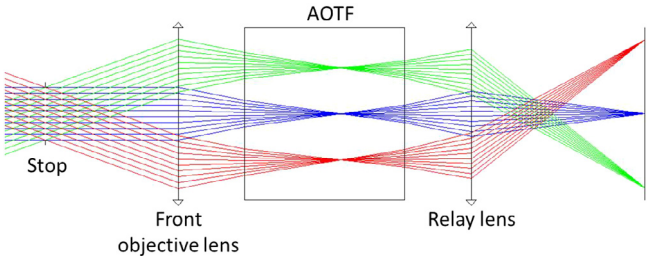

Fig. 6. Optical structure of the imaging spectrometer based on the telecentric beam incident AOTF.

lower requirements for the AOTF aperture and CCD size. The aperture of AOTF we will use is 11 × 12 mm, which is greater than the image height and meets the demand.

In sum, the imaging spectrometer adopts the equidistance projection mode and the optical structure of the telecentric beam incident on the AOTF.

3.3. Front objective lens of the imaging spectrometer

According to the requirements, the front objective lens must be able to detect both the nadir and limb fields of view simultaneously. These two fields of view have different focal lengths, and the limb field of view needs to cover all directions. The catadioptric panoramic imager utilizes a PAL for imaging in a large circular field of view, and its image plane is a ring-shaped image that surrounds the central blind area [12–14]. The imaging coverage of the imager is in line with the limb field of view of the imaging spectrometer. Therefore, we select the folded-back panoramic imaging structure as the front objective of the imaging spectrometer. The traditional PAL of the panoramic imager comprises more than three surfaces with different curvatures [15], which only increase the processing difficulty. In this paper, we use a PAL that comprises two surfaces with different curvatures to receive the light of the limb field of view. We also control the catadioptric properties at different positions of the PAL surfaces by using different films. Fig. 7 shows the structure of PAL. The light of the limb field of view enters PAL in the edge area of surface 1 and is then reflected at internal reflection zones B and A before the existing PAL from the center area of surface 2. To realize the catadioptric function, the ring-shaped reflection films must be plated on reflection zones A and B.

Unlike the traditional panoramic imager, the front objective also detects the nadir field of view. Therefore, PAL also needs to have an imaging function in a small field of view. As seen in Fig. 7, the central

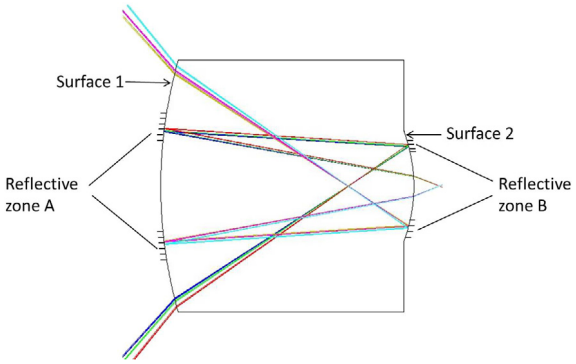

Fig. 7. Panoramic annular lens (PAL)

areas of surfaces 1 and 2 of PAL are light-transmitting regions. The beam of the nadir field of view can enter PAL from the central area of surface 1 and then leave PAL from the central area of surface 2. Meanwhile, the light from the nadir field of view without undergoing reflection processes in PAL. Fig. 8 presents a schematic diagram of the beam transmission of the nadir and limb fields of view in PAL. The curvatures of the front and rear surfaces of the PAL are 0.0245/mm and 0.0721/mm, respectively. And the thickness of the PAL is 22.6 mm, which is made of fused-silica for resist the space radiation.

According to the detection requirements, the nadir and limb fields of view have different focal lengths. In the first design process of the front objective lens, we control the focal length of the front objective lens according the requirements of the limb field of view. After determining the initial structure, we place some correction lenses in front of PAL to correct the focal length and aberration of the nadir field of view. To ensure that both fields of view have the same image telecentricity, the two fields of view use the same stop placed behind the PAL. We control the exit pupil position of the front objective lens at infinity to ensure optical telecentricity. Fig. 9(a) and (b) respectively show the optical structure and prototype of the front objective lens. As Fig. 9(a), the front objective lens have two fields of view, and the nadir light enters the optical system from the correction lenses, while the limb light from PAL. Therefore, the ordinary lens cone block the limb beam. In this design, the lens cone of the optical system adopts a frame structure, that is, the cone with PAL and the cone with correction lenses are connected by mechanical frame. Fig. 10 is the image taken by prototype, it can be seen that the mechanical frame slightly obscures the limb field of view, resulting that some periodic shadows appear on the annular limb image.

3.4. Effect of the AOTF on imaging

The AOTF has great influence on the chromatic aberration and astigmatism of the final image [15]. As shown in Fig. 11, the focus of different spectra will be separated in the axial direction after passing through the crystal because different wavelengths have different refractive indices. If the refractive index of the light in the crystal at a wavelength of λ is n(λ), then the axial movement of the focus after passing through the crystal is

$$d_\lambda = l\left\{1 - \frac{\tan[\arcsin\frac{\sin i}{n(\lambda)}]}{\tan i}\right\}, \tag{7}$$

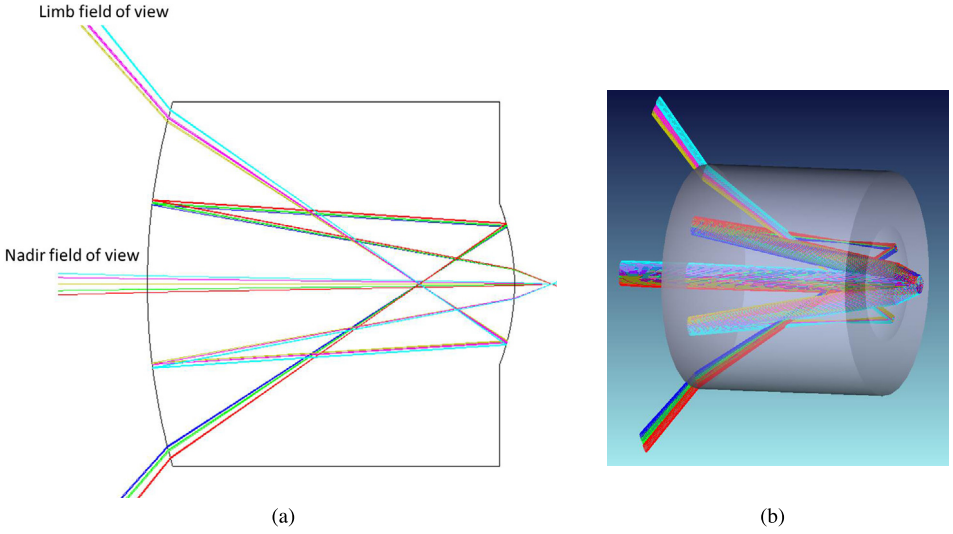

Fig. 8. Schematic diagram of beam transmission in PAL. (a) 2D diagram, and (b) 3D diagram.

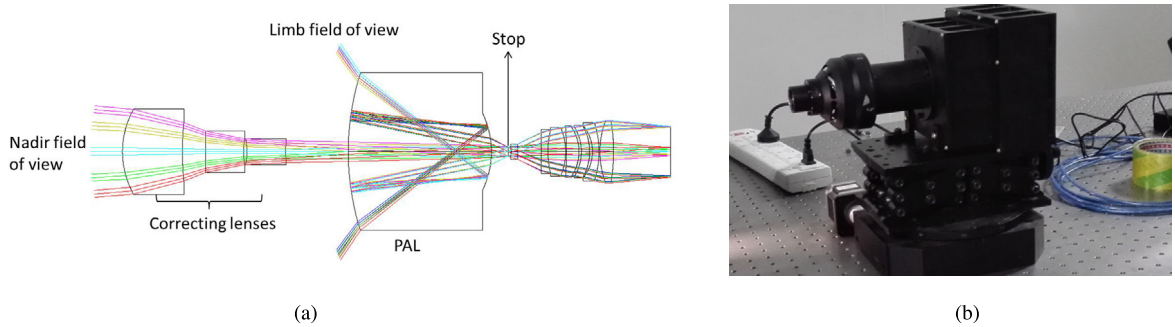

Fig. 9. (a) Optical structure, and (b) the prototype.

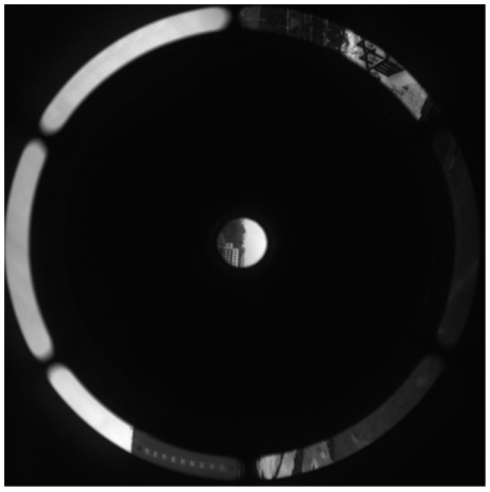

Fig. 10. Image taken by the front objective lens.

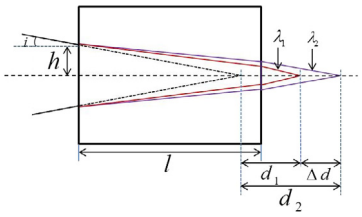

Fig. 11. Chromatic focus shift caused by the AOTF.

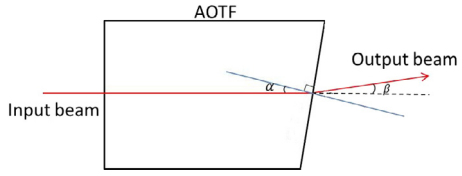

Fig. 12. Simulated diagram of the direction offset of the beam caused by the AOTF.

which can be approximated as

$$d_\lambda = l \cdot [1 - \frac{1}{n(\lambda)}]. \tag{8}$$

Therefore, the longitudinal chromatic aberration of beams λ_1 and λ_2 is

$$\Delta d = l \cdot [\frac{1}{n(\lambda_1)} - \frac{1}{n(\lambda_2)}]. \tag{9}$$

The crystal length in the AOTF is generally long, thereby causing a large chromatic aberration. To ensure the image quality, the relay system must correct the chromatic aberration caused by the AOTF.

The AOTF shifts the beam transmission direction, which in turn has a great influence on astigmatism and seriously affects the imaging quality. Therefore, the beam offset in an optical system must be simulated and corrected. As shown in Fig. 12, the direction offset caused by the AOTF can be simulated by the slight tilt of the second surface of the crystal. By denoting the direction offset angle caused by the AOTF as β, the tilt angle of the rear surface of the crystal can be obtained from the following refraction law:

$$\alpha = \arctan[\frac{\sin\beta}{n(1-\cos\beta)}]. \tag{10}$$

3.5. Relay lens of the imaging spectrometer

The relay lens is responsible for the secondary imaging of the beam split by the AOTF. To prevent changing the focal length of the whole system, a relay lens with a magnification of 1:1 is selected as the initial structure, while the object numerical aperture and object height of the relay system are set to match those of the front objective lens. Given that the AOTF must be placed between the front objective lens and relay lens, the object distance needs to be sufficiently long. Fig. 13 shows the structure of the relay lens. The object distance is 50 mm, which is sufficient for placing the AOTF. The relay system adopts a quasi-symmetrical structure.

3.6. Splicing and optimization of the whole optical system

Given that both the front objective lens and relay lens are telecentric, the two systems can be easily spliced together. The AOTF to be used has a spectral range of 450 nm–800 nm, spectral resolution of 1.5 nm, and spectroscopic crystal of TEO_2. To simulate the chromatic aberration of the AOTF, we add a TEO_2 flat plate with a certain thickness between the front objective lens and relay lens. After adding the TEO_2 crystal, the distance between the front objective lens and relay lens must be adjusted according to Eq. 11 [16]:

$$D = D_1 + D_2 + \frac{T}{N}, \tag{11}$$

where D is the air space before placing the crystal, D_1 and D_2 are the new air spaces between the crystal and the front and relay lenses, respectively, T is the crystal thickness, and N is the crystal refractive index.

The AOTFs are polarization-sensitive optical elements, and the beam entering the AOTF must be linearly polarized according to the use requirements of the AOTF. Therefore, a polarizer must be placed in front of the AOTF. Fig. 14 shows the spliced whole optical system.

The AOTF causes a slight shift in the beam transmission direction. To simulate such beam shift, we set a slight tilt angle on the rear surface of the TEO_2 crystal by following Eq. (9), thereby producing large orders of magnitude astigmatism in the optical system. Given that the optical system of Fig. 13 does not correct the astigmatism generated by the AOTF, the spliced optical system can only be used as an initial structure for further optimization. As shown in Fig. 15, a common method for correcting astigmatism is to add a wedge-compensating lens behind the AOTF to offset the astigmatism between the wedge compensation lens and the AOTF. We use this method to further optimize the optical system.

The optical system has two structures, namely, nadir and limb. Optimizing these two structures together will greatly reduce the optimization speed of the software. Therefore, we initially optimize the limb structure. If only the limb large field of view is optimized, then the astigmatism and chromatic aberration of the nadir small field of view tend to be poorly corrected. Therefore, when optimizing the limb structure, several virtual small fields of view similar to the nadir field of view in the limb structure must be added. In practical imaging, these virtual small fields of view are meaningless. However, in the optimization process, these virtual fields of view can ensure that the astigmatism and chromatic aberration of the small field of view are well corrected. Given that astigmatism and chromatic aberration are generated by the AOTF, only the system after the AOTF is optimized during the optimization process. The optimization variable includes the tilt angle of the wedge compensation lens and all the radii, materials, and thicknesses in the relay lens. Fig. 16 shows the re-optimized limb structure. The relay lens of the spectrometer loses its symmetry because it needs to balance the aberrations caused by the front objective lens and the AOTF.

Given that the center virtual field of view is added to the limb structure in the optimization process, the relay lens also has a relatively good correction effect on the astigmatism and chromatic aberration of the nadir small field of view. Afterward, the correcting lenses are added before the PAL to control the focal length and to further reduce the aberration of the nadir field of view. Fig. 17 shows the optical system of the nadir and omnidirectional limb imaging spectrometer.

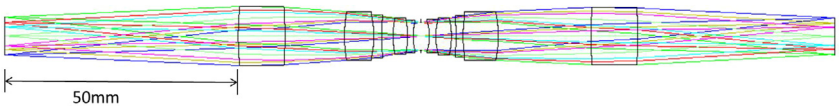

Fig. 13. Initial optical structure of the relay lens.

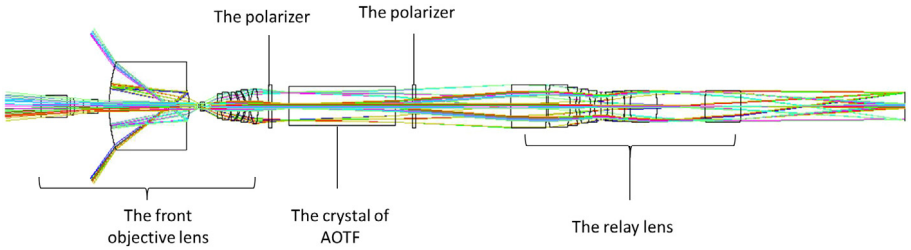

Fig. 14. Spliced whole optical system.

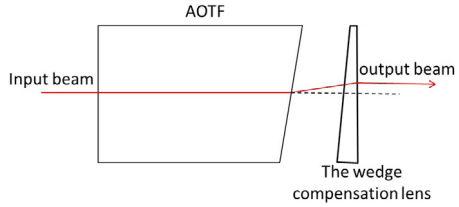

Fig. 15. Combination system of the AOTF and wedge compensation lens.

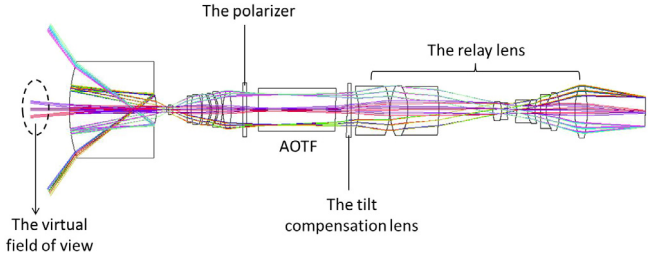

Fig. 16. Re-optimized limb structure.

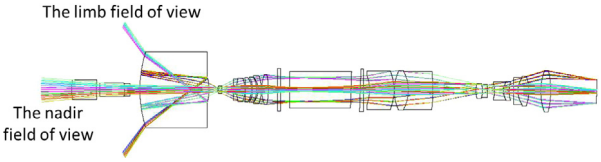

Fig. 17. Optical system of the nadir and omnidirectional limb imaging spectrometer.

4. Image quality analysis

Given that the CCD detector to be used has a pixel size of 13 μm, the Nyquist frequency of the detector is 38.5 lp/mm. MTF can comprehensively evaluate the imaging quality of the optical system. The polychromatic MTF of the optical system is shown in Fig. 18, where (a) is the nadir field of view and (b) is the limb field of view. The MTF of the nadir field of view is greater than 0.54@38.5 lp/mm, while that of the limb field of view is greater than 0.6@38.5 lp/mm. The contrast of the image satisfies the imaging requirements.

Unlike ordinary imaging instruments, the imaging spectrometer must perform imaging in different spectral segments. Moreover, the polychromatic MTF cannot estimate the contrast of a single spectral. Therefore, we must also check the monochromatic MTF of the spectrometer. Fig. 19 shows the monochromatic MTF of the nadir field of view

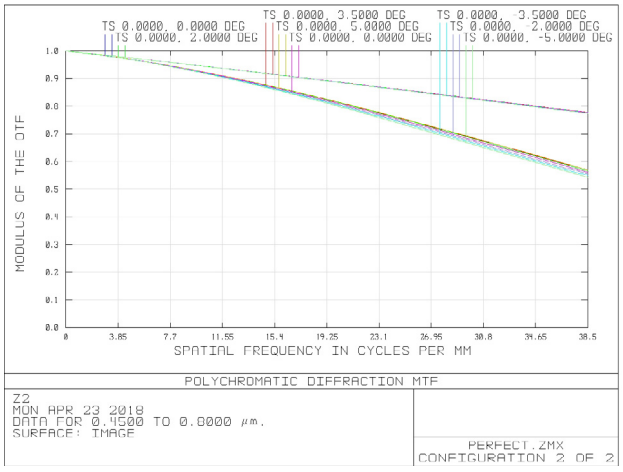

(a)

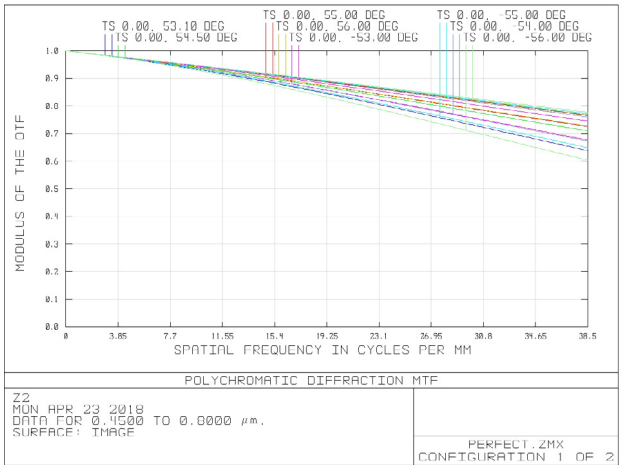

(b)

Fig. 18. Polychromatic MTF of the optical system. (a) Nadir field of view, and (b) limb field of view.

and reveals that the MTF of each band is greater than 0.7@38.5 lp/mm. Meanwhile, Fig. 20 shows the monochromatic MTF of the limb field of view and reveals that the MTF of each band is greater than 0.5@38.5 lp/mm. Each band in the two fields of view shows good contrast.

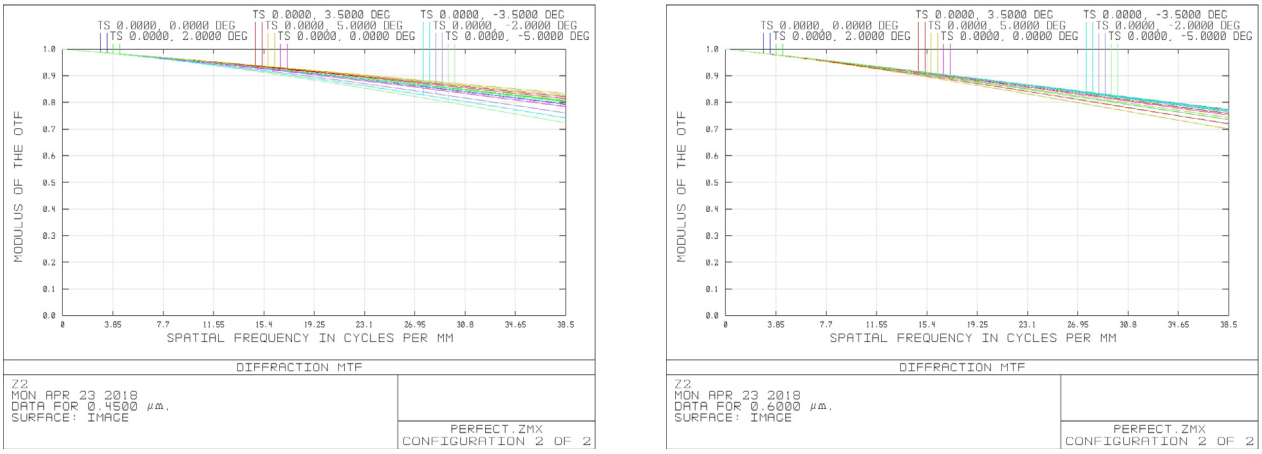

Fig. 19. Monochromatic MTF of the nadir field of view. (a) to (c) 450, 600, and 800 nm, respectively.

As an imaging system, the distortion of the spectrometer must be controlled within a reasonable range. The system considers the F-Theta projection relationship, and Fig. 21 shows the field curvature and distortion of the nadir field of view. The field curvatures of all bands are below 0.06 mm, and the maximum distortion is less than 0.03%.

Given that the limb field of view of the optical system is 360° × (53.1°–56°), the (0°–53.1°) field of view is invalid. Therefore, the distortion values and changes cannot be intuitively viewed from the optical design software. In this case, we use the operand "RAGY" to read the imaging position Y_r of the different fields of view from the ZEMAX software and calculate the distortion of the limb field of view as

$$Dis = \frac{Y_r - f \cdot \theta}{f \cdot \theta} \times 100\%, \tag{12}$$

where f is the focal length of the limb structure, and θ is the field of view. We collect the positions of 11 field points at equal intervals before calculating the distortion values and fitting the distortion curve of the limb field. Fig. 22 shows that the distortion is approximately linear with the field of view and that the distortion at the maximum field of view is less than 0.42%, which is lower than the highest distortion of the design specifications.

5. Calibrations method for the spectrometer

Generally, spectrometers calibration includes spectrum calibration and radiation calibration. Compared with the wavelength dispersion spectrometers, the AOTF as a spectroscopy device is used in the self-developed spectrometer. In addition, there is a relationship between the output spectrum and input electrical signal of the AOTF, and which is able to be verified by wavemeter. Therefore, a traditional spectrum calibration process is not suitable.

In the calibration process, calibrations for two limb fields at same time cannot be realized because the nadir and limb fields have different focal lengths. In order to achieve the desired calibration performance, the integrating sphere is used to calibrate the nadir and limb fields separately. The calibrations schematic diagram is shown in Fig. 23, (a) and (b) are the calibration diagrams of the nadir field and limb field, respectively. The calibration factors can be calculated based on the radiance emitting from the opening cell on the integrating sphere and the digital number output from the CCD detector. When the calibration of a certain field of view is processing, the light baffle is used to block another field of view to avoid influence from stray light.

6. Conclusion

We introduce the spectroscopic principle of the AOTF to deduce the diffraction equation and analyze the aberration of the AOTF. By using the AOTF as a spectroscopic device, we also design a spectrometer that can simultaneously detect the image and spectral information of the nadir and limb fields of view. This spectrometer comprises a front

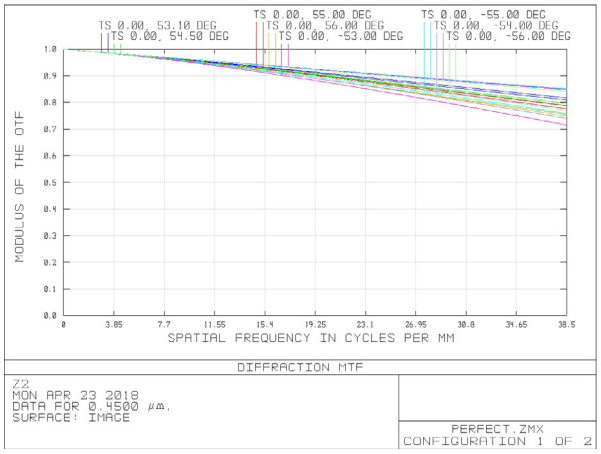

(a)

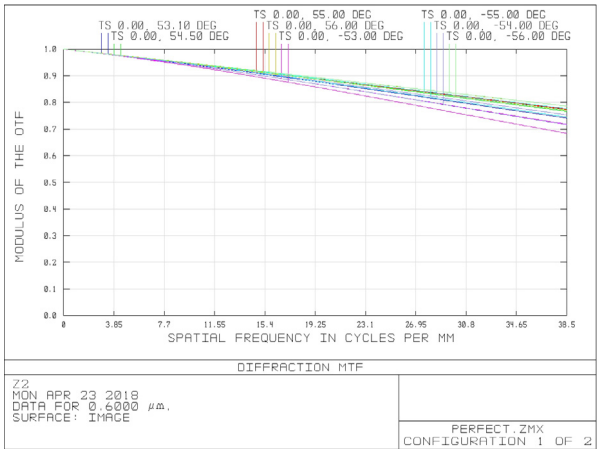

(b)

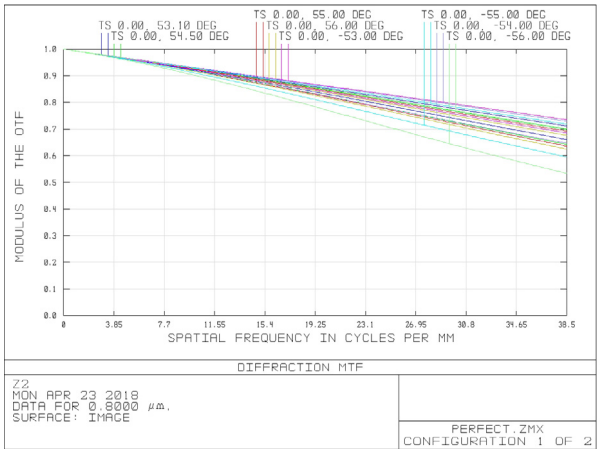

(c)

Fig. 20. Monochromatic MTF of the limb field of view. (a) to (c) 450, 600, and 800 nm, respectively.

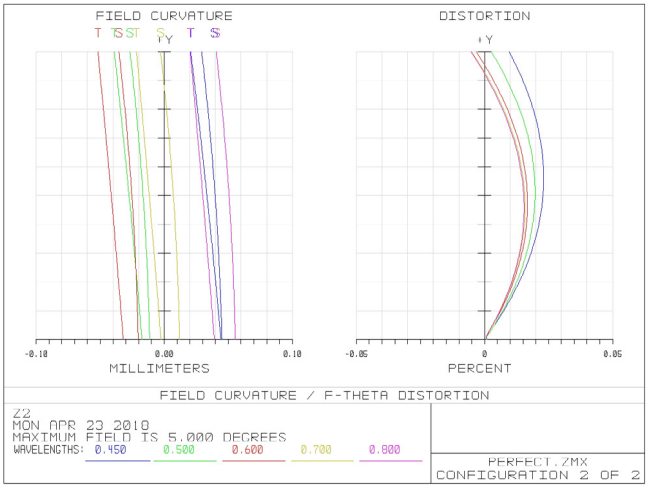

Fig. 21. Field curvature and distortion of the nadir field of view.

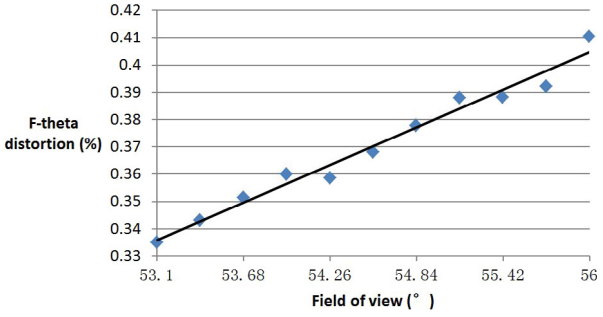

Fig. 22. Distortion of the limb field of view.

objective lens, an AOTF spectroscopy system, and a relay lens. The front objective lens uses a multi-functional PAL to simultaneously detect two fields of view. We place three correction lenses in front of the PAL to correct the focal length and aberration of the nadir field of view. The optical system has a higher detection efficiency and a better atmospheric detection ability compared with the existing atmospheric detection equipment with single mode and single detection.

Funding

Youth Innovation Promotion Association, Chinese Academy of Science; National Science Foundation for Young Scholars of China (61505203); National Key Research and Development Plan of China (2016YFB0502605)

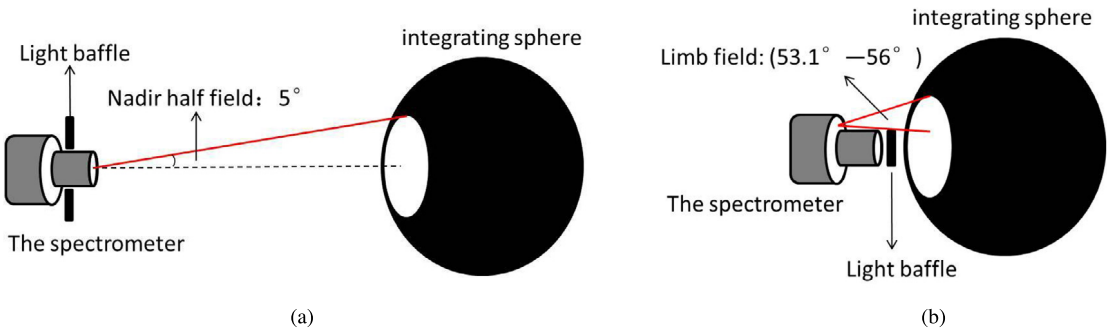

Fig. 23. Radiation calibrations for the spectrometer. (a) Nadir field of view, and (b) limb field of view.

References

[1] L. Yu, Upgrade of a UV–VIS-NIR imaging spectrometer for the coastal ocean observation: concept design, fabrication, and test of prototype, Opt. Express 25 (13) (2017) 15526–15538.

[2] C. Montero-Orille, X. Prieto-Blanco, H. González-Núñez, R. de la Fuente, Two-wavelength anastigmatic Dyson imaging spectrometers, Opt. Lett. 35 (14) (2010) 2379–2381.

[3] R. Allured, R.L. Mcentaffer, E. Hertz, P.N. Cheimets, R.K. Smith, Optical design considerations and raytracing results for the Arcus grating spectrometer concept, Proc. SPIE. 9905 (2016) 99054O.

[4] H.G. Werij, C. Olij, A.E. Zoutman, A. Kamp, SCIAMACHY: the completion of a new-generation instrument for studying the atmosphere, Proc. SPIE. 2957 (1997) 20–30.

[5] D.L. Wu, P. Preusse, S.D. Eckermann, J.H. Jiang, M.D.L.T. Juarez, L. Coy, D.Y. Wang, Remote sounding of atmospheric gravity waves with satellite limb and nadir techniques, Adv. Space. Res. 37 (12) (2006) 2269–2277.

[6] X. Wang, Q. Xue, Optical system design of an atmospheric detector with nadir view and omnidirectional limb view, Appl. Opt. 56 (26) (2017) 7454–7461.

[7] C. Zhang, H. Wang, Y. Yang, Z. Zhang, Design and analysis of a noncollinear acousto-optic tunable filter, Opt. Lett. 32 (16) (2007) 2417–2419.

[8] N. Gupta, R. Dahmani, S. Choy, Acousto-optic tunable filter based visible- to near-infrared spectropolarimetric imager, Opt. Eng. 41 (5) (2002) 1033–1038.

[9] G. Fulton, G. Horlick, AOTFs as atomic spectrometers: basic characteristics, Appl. Spectrosc. 50 (7) (1996) 885–892.

[10] H. Zhao, Z. Wang, G. Jia, Y. Zhang, Z. Xu, Chromatic aberrations correction for imaging spectrometer based on acousto-optic tunable filter with transducers, Opt. Express 25 (20) (2017) 23809–23825.

[11] D.R. Suhre, L.J. Denes, N. Gupta, Telecentric confocal optics for aberration correction of acousto-optic tunable filters, Appl. Opt. 43 (6) (2004) 1255–1260.

[12] Y. Huang, Z. Liu, Y. Fu, H. Zhang, Design of a compact two-channel panoramic optical system, Opt. Express 25 (22) (2017) 27691–27705.

[13] T. Ma, J. Yu, P. Liang, C. Wang, Design of a freeform varifocal panoramic optical system with specified annular center of field of view, 19(5)(2011) 3843–3853.

[14] J. Wang, Y. Liang, M. Xu, Design of panoramic lens based on ogive and asperic surface, Opt. Express 23 (5) (2015) 19489–19499.

[15] X. Zhou, J. Bai, C. Wang, X. Hou, K. Wang, Comparison of two panoramic front unit arrangements in design of a super wide angle panoramic annular lens, Appl. Opt. 55 (12) (2016) 3219–3225.

[16] M. Laikin, Lens Design, fourth ed., Taylor & Francis Group, 2006, Chap. 1.